Catalysis Science & Technology

ROYAL SOCIETY OF CHEMISTRY

COMMUNICATION

View Article Online
View Journal | View Issue

Cite this: *Catal. Sci. Technol.*, 2026, **16**, 3137

Received 14th February 2026,
Accepted 21st March 2026

DOI: 10.1039/d6cy00192k

rsc.li/catalysis

Enhanced N_2 capture and cleavage promoted by lithium nanoparticles

José Miguel Doña-Rodríguez, [a] Raúl Quesada-Cabrera, [a] Douglas R. MacFarlane, [b] Alexandr N. Simonov *[b] and Luis Miguel Azofra *[a]

Activation of N_2 with metallic lithium is a key step of the lithium redox-mediated nitrogen reduction reaction (Li-NRR) – a process that can enable practical ammonia electrosynthesis under mild conditions. Our present DFT study revealed that N_2 capture and N≡N bond cleavage is substantially enhanced on and within Li^0 nanoparticles as compared to bulk slabs. This behaviour is not limited to single-molecule adsorption but is also observed during the successive capture of additional N_2 molecules. The results presented herein might assist in the design of higher performance Li-NRR systems.

The nitrogen reduction reaction (NRR) is one of the most extensively studied processes of the last decade in the field of applied electrocatalysis, owing to the importance of ammonia as a fertiliser feedstock and a future energy vector.[1] However, research on the electrochemical N_2 activation under mild conditions has demonstrated that the direct electrocatalytic reduction of N_2 is challenging to achieve at production rates that are viable on a practical scale.[2] In contrast, the lithium redox-mediated NRR (Li-NRR) has been unambiguously proven to provide practical levels of genuine conversion of N_2 into NH_3 at ambient temperature and mild pressure <20 bar.[3–7]

In the Li-NRR, the electrochemically generated metallic lithium mediates N_2 cleavage with the formation of lithium nitride *via* a dissociative mechanism, which demonstrates a range of distinctive features[8–10] as compared to the mechanisms of N_2 activation proposed for the direct electrocatalytic NRR.[11–18] Next, the nitrogen atoms incorporated into the Li_3N lattice are converted into NH_3 through successive protonation by a suitable proton carrier.[19,20] A similar mechanism has recently been reported for calcium[21] and magnesium.[22]

At a theoretical level, this behaviour has been modelled in metal slabs, in the first instance for the N_2 cleavage mechanism (Fig. 1),[8–10] but also in subsequent protonation steps.[23,24] These previous studies established that: (i) end-on adsorption of N_2 on Li^0 is non-spontaneous; (ii) side-on adsorption, by contrast, is spontaneous, overcoming the physisorption regime, as N_2 becomes inserted into the surface structure of the Li^0 slabs, with binding free energies characteristic of chemisorption or capture events; (iii) N_2 can diffuse into the inner layers of the Li^0 bulk; and (iv) the activation free-energy barriers for N_2 cleavage on the Li^0 surface or within the Li^0 bulk are accessible at room temperature.

However, metal slabs represent restricted structures, in contrast to nanoparticles which exhibit diverse structural features, like different facets as well as edges and corners. These features are likely relevant to the real state of the electroplated Li^0 intermediate during the Li-NRR, since electrodeposition of lithium metal typically produces highly heterogeneous nanostructured aggregates rather than well-

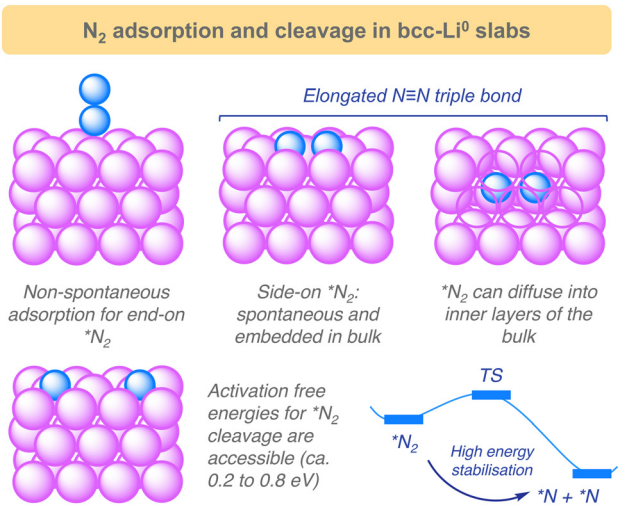

Fig. 1 Summary of the main chemical events observed during the N_2 capture and cleavage on and within the bcc-Li^0 slabs.[8,9]

[a] *Instituto de Estudios Ambientales y Recursos Naturales (i-UNAT), Universidad de Las Palmas de Gran Canaria (ULPGC), Campus de Tafira, 35017 Las Palmas de Gran Canaria, Spain. E-mail: luismiguel.azofra@ulpgc.es*
[b] *School of Chemistry, Monash University, Clayton, Victoria 3800, Australia. E-mail: alexandr.simonov@monash.edu*

defined crystalline surfaces.[25–27] To investigate this, we conducted a density functional theory (DFT) study (pseudopotential plane-wave method, RPBE[28] + D3[29,30] level of theory, VASP,[31–34] see SI, for computational details) of a series of structures that were modelled by spherically projecting the body-centred cubic (bcc) Li^0 unit cell with radii ranging from 1 to 6 Å. This resulted in a series of initial models: the Li_1 atomic dot (1 Å radius), the Li_2 (2 Å), Li_6 (3 Å), Li_{15} (4 Å) and Li_{27} (5 Å) sub-nanoclusters, and the Li_{51} (6 Å) nanoparticle (Fig. 2).

In our previous study on the interaction of N_2 on and within the bcc-Li^0 slabs, we computed binding free energies for the (001) and (011) flat surfaces, amongst others.[8,9] We found that end-on N_2 adsorption exhibited non-spontaneous values of 0.22 eV in both cases, whereas side-on adsorption was spontaneous, with values of −0.46 and −0.66 eV, respectively. The computational protocol used in that study differs from the one employed herein in the calculation of vibrational frequencies only, where atomic positions of the metal were frozen in the previously published work.[8,9] While slabs can be considered constrained structures due to their periodicity, this assumption does not hold for nanostructures. Consequently, when recalculating the side-on N_2 binding on the (001) and (011) facets without structural constraints in the frequency calculation, the values changed slightly to −0.35 and −0.55 eV, respectively. By applying a consistent methodology, comparison of the N_2-adsorption results computed here for our sub-nanoclusters and nanoparticle models with those for metal slabs was therefore straightforward.

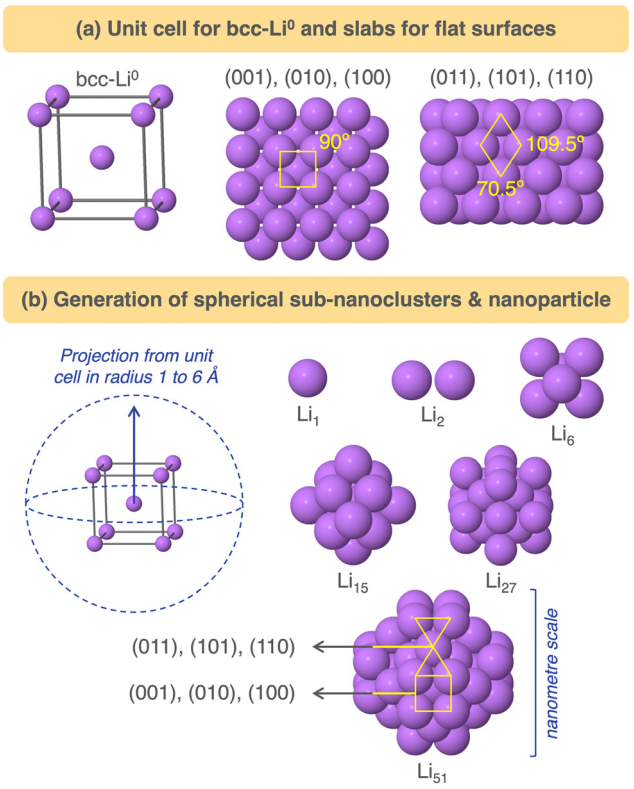

Fig. 2 (a) Most common flat surfaces (top view) of bcc-Li^0: (001), equivalent to (010) and (100), and (011), equivalent to (101) and (110). (b) Generation of sub-nanoclusters and nanoparticle models *via* spherical projection of the bcc-Li^0 unit cell, resulting in Li_1 (radius, r = 1 Å), Li_2 (r = 2 Å), Li_6 (r = 3 Å), Li_{15} (r = 4 Å), Li_{27} (r = 5 Å), and Li_{51} (r = 6 Å).

Interestingly, both Li_1 and Li_2 – the simplest models examined herein – exhibited highly non-spontaneous N_2 binding free energies (ΔG_b). For instance, the linear end-on minima (labelled [1] in both cases in Fig. 3) showed ΔG_b values of 0.36 and 0.34 eV, respectively, along with minimal N≡N bond elongations of 0.03 and 0.01 Å, compared with the nitrogen–nitrogen distance of 1.12 Å for $N_2(g)$ obtained using this computational protocol. These energy values were similar or even less favourable than those others considered herein, specifically minimum [2] for Li_1 of side-on type (0.54 eV), and minima [2] and [3] for Li_2 of angular end-on (0.31 eV) and side-on (0.55 eV) types.

In principle, these results qualitatively follow the trends established before for the Li^0 slabs, where the side-on adsorption was energetically more favourable than end-on.[8,9] However, it was somewhat surprising to find that the interactions between N_2 and these Li^0 structures were so endergonic, given that both Li_1 and Li_2 represent single-site models. Indeed, single-site models have demonstrated superior substrate-interaction capabilities for many other systems. For example, this was shown for the end-on interaction of N_2 with iron slabs[35] and with a single iron atom,[36] where the binding energy in the latter case increases by nearly a factor of seven, although we acknowledge that, in this model, the single-site iron atom was not isolated but supported on a MoS_2 sheet. However, in the case of Li^0, energetically favourable N_2–metal interactions seem to demonstrate an opposite trend.

Li_6 formally represents a cluster-type structure of a square-based bipyramid. In this case, we observe binding events that deviate from the general trend in N_2-philicity exhibited by Li^0 slabs. Four minima were identified for this model: the linear end-on minimum, labelled [1], was slightly physisorbed with a spontaneous ΔG_b (*ca.* −0.1 eV), whereas ΔG_b values were endergonic for minima [2]–[4], despite [2] and [3] being side-on (the former interacting with three Li centres and the latter with two) (Fig. 3).

Note that two binding free energy values are reported for all lithium models, except Li_1 and Li_2, considered herein because, unlike metallic slabs, they undergo distortions relative to their original structures. The first ΔG_b value refers to the free energy difference between the minimum in question and the perfectly symmetric cluster. The second ΔG_b was calculated by re-optimising the cluster structure after removal of the adsorbed N_2 molecule. The difference between the two values provides a measure of the energy associated with cluster structure deformation. It should be noted that the deformation energy discussed herein does not necessarily reflect stability of Li^0 nanostructures during Li-NRR. A proper assessment of this aspect would require a separate investigation involving additional species participating in the reaction.

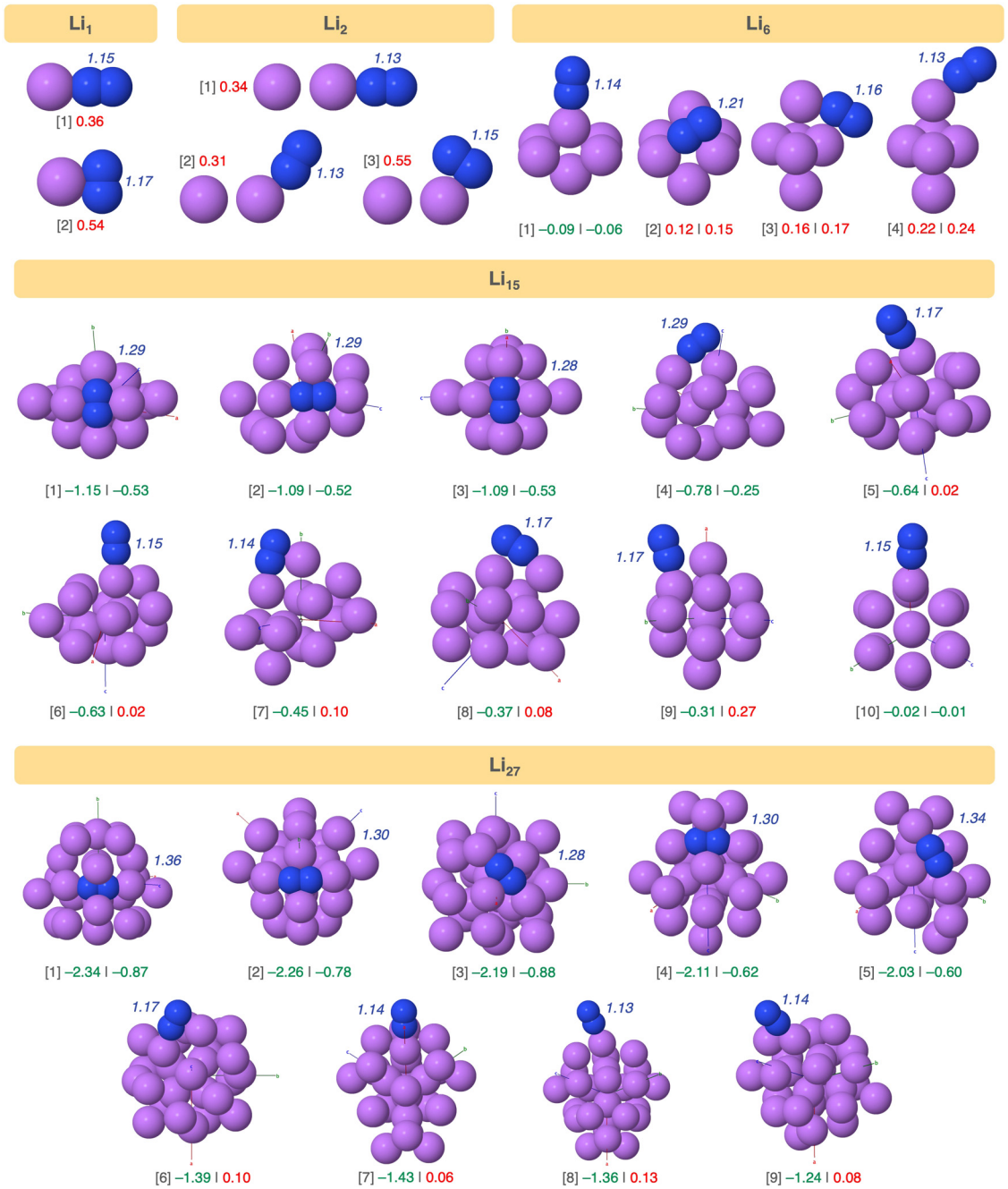

Fig. 3 *N_2 minima obtained for the Li_1 atomic dot and the Li_2, Li_6, Li_{15}, and Li_{27} sub-nanoclusters. N≡N distances (in Å) are shown in *blue*. Binding free energies (in eV) are indicated in green for spontaneous and red for non-spontaneous values. For the Li_{15} and Li_{27} models, Cartesian axes (*a*, *b*, *c*, corresponding to OX, OY, and OZ, respectively) are also shown as a reference for orientation, facilitating comparison with the symmetric structures presented in Fig. 2.

For the Li_6 cluster, this difference was negligible, meaning almost no deformation with respect to the perfectly symmetrical cluster of this type (Fig. 3). In contrast, the change was pronounced for the Li_{15} model, where the cluster deformation energies were, in most cases, around −0.6 eV; that is, the distorted structures were more stable than the initial perfectly symmetric cluster. From the perspective of formal analysis of N_2 stabilisation, it is the second ΔG_b value that is of major interest.

For Li_{15}, the binding free energies of N_2 were similar to those computed for the slabs, with values of −0.53, −0.52, and −0.53 eV for the first three minima, which: (i) are of side-on type; (ii) correspond to molecules embedded within the cluster surface; and (iii) show that superficial interactions lead to the decreased ΔG_b values (Fig. 3). We also observed that the captured N_2 molecules in these more stable configurations were activated, with elongated N≡N bonds to approximately 1.3 Å. Although the ΔG_b values for these three

most stable minima were similar, their electronic energies, *i.e.*, not including enthalpic and entropy contributions, differed by more than 0.1 eV (≈9.65 kJ mol^{-1}), confirming that they represent distinct structures on the potential energy surface (PES).

The binding free energy results for the Li_{27} model further emphasised the intensification of the N_2–Li^0 interactions within atom clusters as compared to the slab models. We identified a series of side-on and embedded N_2 minima, labelled [1]–[5], whereas minima [6]–[9] correspond to mixed ([6]), angular ([7]), and linear end-on ([8]–[9]) types (Fig. 3). For the former (side-on), ΔG_b was exergonic, while for the latter (mixed and end-on) it was not. This behaviour, although somewhat expected, would not be particularly noteworthy if the N_2 binding free energy values did not significantly exceed the reference values obtained for slabs (−0.55 eV). In these clusters, the interactions reached as much as −0.9 eV, indicating that N_2 capture was strongly enhanced, accompanied by substantial activation of the molecule. For instance, for side-on minima [1]–[5], N≡N bond lengths ($r_{N\equiv N}$) elongated up to 1.28–1.36 Å (Fig. 3).

To explore if this improved N_2 fixation could be maintained, and to what extent, at the nano- rather than sub-nanometre scale discussed above, we further studied the Li_{51} nanoparticle model. The intensity of N_2 capture in Li_{51} followed a pattern similar to that observed in the Li_{27} cluster: side-on and embedded N_2 structures on the nanoparticle surface exhibited ΔG_b values ranging from −0.88 eV for the most stable to −0.60 eV for the least stable, whereas end-on interactions remained endergonic. This is exemplified in Fig. 4a for the three most stable N_2 minima identified for the Li_{51} model, with the remaining minima provided in Fig. S2. Notably, the N≡N bond elongation was slightly greater than that observed for the corresponding minima in the Li_{27} model, and distortion energies were somewhat higher, indicative of enhanced stability in the non-symmetric Li_{51} nanoparticle compared with the symmetric structure (*cf.* data in Fig. 3 and 4a). A correlation between ΔG_b and the number of lithium atoms interacting with N_2 was noted for $*N_2$ minima in both the Li_{27} and Li_{51} models (Fig. S5), consistent with our observation that binding free energy became stronger as the number of the Li···N bonds increased.

In light of these results obtained for the larger nanostructures, Li^0 appears to exhibit a pronounced affinity towards N_2. Nevertheless, further investigations including explicit solvent molecules will be required to evaluate possible competitive adsorption effects under more realistic conditions.

Further, we sought to explore fundamental aspects of the N_2 cleavage mediated by the lithium metal nanoparticle by addressing two questions: (i) what is the energy cost (activation barrier) associated with cleaving the $*N_2$ molecule into N adatoms (*N) during the formation of lithium nitride; and (ii) is capture of a second N_2 molecule also an energetically favourable process?

Addressing the first question, the computed activation energies for the lithium-mediated dinitrogen dissociation process were low to moderate, that is, with values less than 1

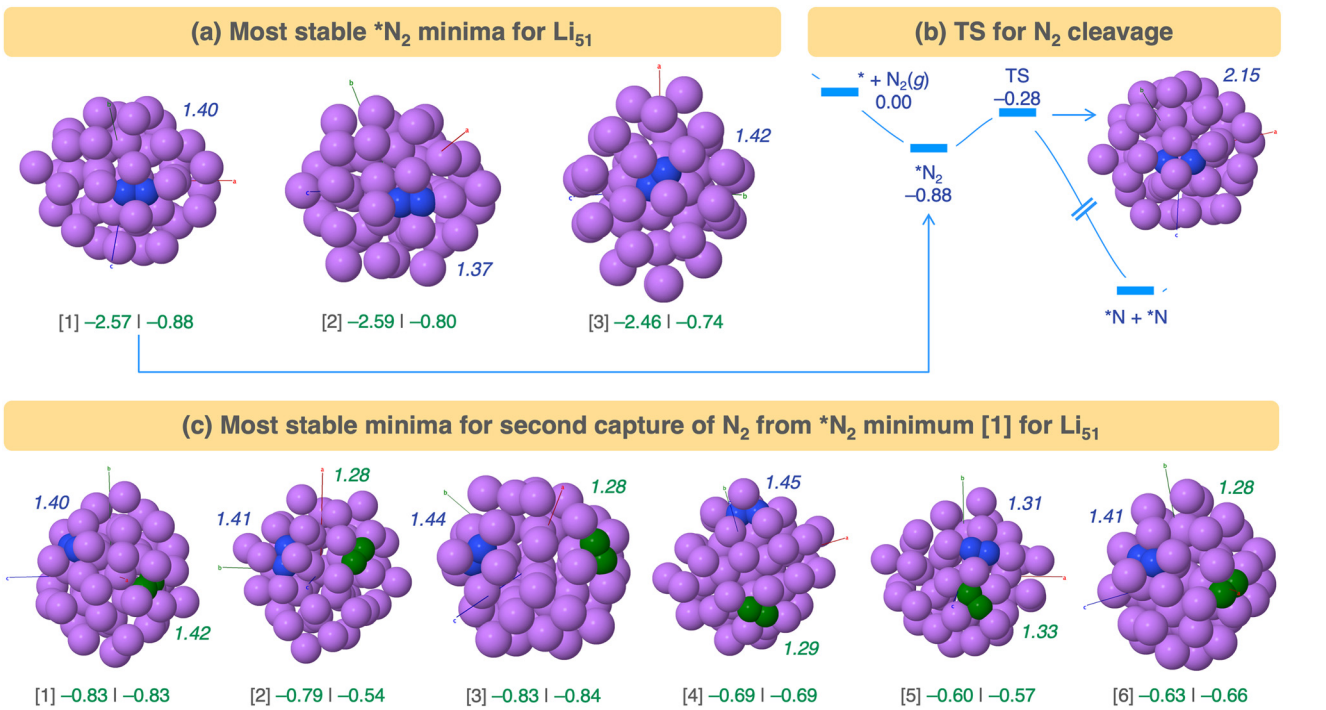

Fig. 4 (a) Most stable $*N_2$ minima (all side-on) obtained for the Li_{51} nanoparticle. (b) Potential energy surface (PES) for N_2 capture and cleavage of minimum [1] in the Li_{51} model, including the optimised structure of the N≡N cleavage transition state. (c) Most stable minima for a second N_2 capture, where the original $*N_2$ from minimum [1] is shown in blue and the second $*N_2$ in green. N≡N distances (in Å) are shown in *italics*, following the same colour code.

eV. Specifically, we performed calculations to locate the transition states (TSs) for N_2 cleavage of the six most stable side-on N_2 minima in the Li_{51} model, obtaining values ranging from 0.46 eV for the lowest barrier to 0.64 eV for the highest (Table S3 and Fig. S3). Remarkably, all activation barriers were smaller, in absolute terms, than the energy released upon N_2 chemisorption. This is exemplified in Fig. 4b for the minimum [1] of the Li_{51} model. In this case, the * + $N_2(g)$ → *N_2 physical process exhibited a free energy drop of −0.88 eV, as discussed previously, and an activation barrier of 0.61 eV relative to this state. Additionally, the chemisorbed N_2 molecule showed a bond elongation of 0.28 Å ($r_{N\equiv N}$ = 1.40 Å), while the nitrogen–nitrogen distance in the TS was 2.15 Å.

To assess the kinetic accessibility of the embedded N_2-in-Li^0 configurations, a constrained approach scan was performed for the Li_{51} model in which the distance between the central Li atom and N_2 was progressively reduced while relaxing the remaining degrees of freedom (see Fig. S6). The resulting profile reveals a very small electronic energy barrier of 0.14 eV for N_2 penetration into the subsurface region, followed by stabilisation of the embedded state. This indicates that subsurface incorporation is kinetically accessible within the capabilities of the static DFT approach employed herein.

To explore the capability of a lithium nanoparticle to activate multiple dinitrogen molecules, a second N_2 was randomly placed at various positions onto the *N_2 minimum [1] of the Li_{51} model. The capture of an additional N_2 molecule was found to be spontaneous, with structural distortion energies being practically negligible. In more detail, Fig. 4c shows six of the nineteen minima identified for this case, while the remaining structures are provided in Fig. S4. Notably, for all these minima, the second N_2 molecule adopted a side-on configuration in the most stable structures (shown in green in Fig. 4c), with spontaneous ΔG_b values generally comparable to those computed for the first captured N_2 molecule (blue in Fig. 4c). Although the N≡N bond in the second N_2 molecule was also elongated, the magnitude of this effect was less pronounced. By contrast, for all these minima, the bond elongation of the first captured N_2 molecule was maintained or even enhanced, with N≡N distances exceeding 1.4 Å in some cases (Fig. S4).

Based on these results, Li^0 nanoparticles can be considered exceptionally effective N_2 capturers, even more effective than the slab models. To further support this conclusion, we performed NVT [substance (N), volume (V), temperature (T); canonical ensemble] molecular dynamics (MD) simulations starting from an initial configuration in which thirty-six N_2 molecules were positioned in an end-on orientation, pointing towards each of the surface lithium atoms of the Li_{51} nanoparticle and placed at a distance of 3 Å. This setup established unfavourable initial conditions, namely, N_2 molecules at distances corresponding to non-adsorptive interactions and in an end-on orientation, which, as confirmed by our calculations, were non-spontaneous. If the Li_{51} nanoparticle indeed behaves as a highly potent N_2 capturer, the MD simulation could be expected to evolve towards spontaneous adsorption and activation.

The results in this regard were highly instructive. On the picosecond timescale, a progressive insertion of numerous N_2 molecules onto and within the nanoparticle was observed (Fig. 5). As the MD simulation progressed, convergence of the centres of mass of the N_2 molecules with those of the Li^0 atoms was found, indicating the point of interaction between dinitrogen and the lithium nanoparticle surface. Specifically, a substantial number of N_2 molecules were captured within inner layers of Li_{51} after approximately 1.5 ps of the total 4 ps simulation. Throughout this evolution, up to nearly 4 ps, N_2 capture by the Li^0 nanoparticle was accompanied by a decrease in the electronic energy (shown in dark red in Fig. 5), indicating that these adsorption events were

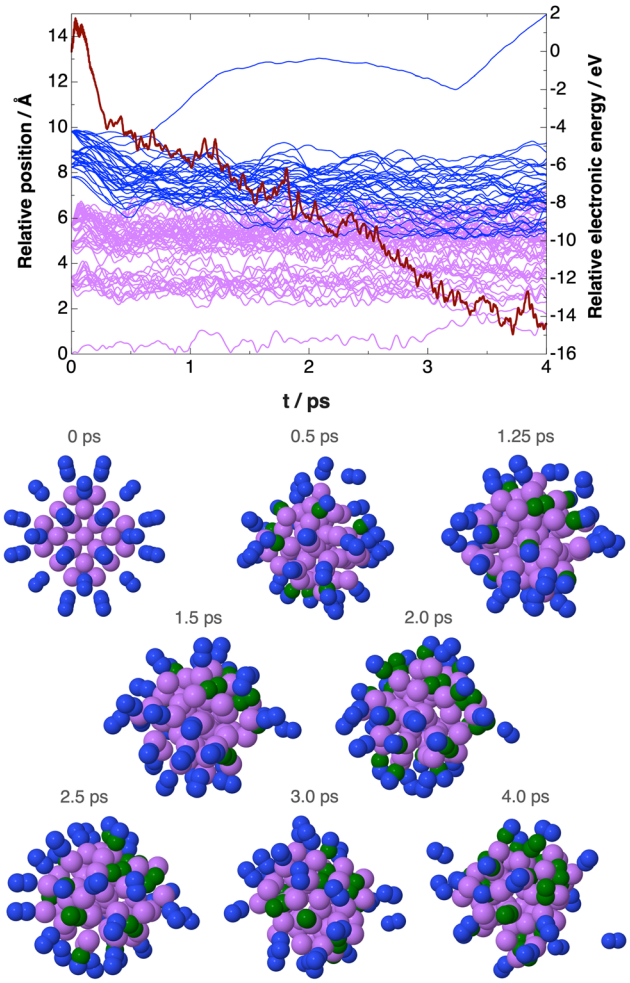

Fig. 5 NVT molecular dynamics for the Li_{51} nanoparticle model surrounded by thirty-six N_2 molecules, each initially placed 3 Å away from the closest N atom interacting with Li. Relative positions (in Å) correspond to the distance of each Li atom (purple) and the centre of mass of each N_2 molecule (blue) relative to the nanoparticle's centre of mass. Evolution of electronic energy (dark red, in eV) is also shown, together with selected snapshots along the NVT MD trajectory. In these structures, N atoms of the N_2 molecules that are closer to the nanoparticle's centre of mass than the outermost Li^0 atom are highlighted in green.

energetically stabilising. Fig. 5 also includes selected snapshots along the MD trajectory, visually illustrating the progressive N_2 capture behaviour of the lithium nanoparticle.

The findings discussed above provide new insights into the chemistry governing the first critical step of the Li-NRR, *viz.* activation of dinitrogen. In the future, it will be important to investigate how the cleavage of a sufficiently large number of captured N_2 molecules ultimately leads to nitridation of the Li^0 nanoparticles. Simultaneous capture of multiple N_2 molecules by the Li^0 nanoparticles may introduce electronic interactions between adsorbates, which could influence the activation of subsequent N_2 molecules. Of an even higher interest is the location of the nitride formation, *viz.* at the surface or in the bulk of the particles, which might result in very different scenarios. Indeed, formation of a lithium nitride surface layer may potentially passivate Li^0 and suppress subsequent N_2 capture. On the contrary, formation of the lithium nitride in the bulk, which might be possible owing to the N_2 diffusion through Li^0 demonstrated herein and previously,[8–10] might allow for the most effective utilisation of the electrochemically generated lithium metal. A detailed assessment of these effects would require a more extensive exploration of the system and is left for future investigation.

Conclusions

In summary, our DFT investigation demonstrated that Li^0 sub-nanoclusters and especially nanoparticles exhibit a remarkable capability for N_2 capture and activation, surpassing that of the previously studied metal slabs. Our calculations revealed that side-on and embedded adsorption configurations lead to significant elongation of the N≡N bond and accessible activation barriers for cleavage, and that multiple N_2 molecules can be captured successively. NVT molecular dynamics simulations indicate that the highly energetically favourable capture events take place on a picosecond scale, with N_2 molecules progressively inserted into the nanoparticle's inner layers. These findings highlight the unique mechanistic role of Li^0 nanostructures in the lithium redox-mediated nitrogen reduction reaction and suggest that such nanoparticles may serve as highly efficient platforms for ammonia synthesis under mild electrochemical conditions. Overall, this study provides fundamental insights into the interplay between size, structure, and reactivity against N_2 of lithium metal, opening new avenues for the design of Li-NRR catalysts.

Conflicts of interest

J. M. D.-R., R. Q.-C., and L. M. A. declare no conflicts of interest. D. R. M. and A. N. S. declare competing financial interests since they are shareholders in Jupiter Ionics Pty Ltd, a start-up company focused on commercialising ammonia production technology.

Data availability

The material presented herein does not possess any characteristics that require additional guidance regarding its findable, accessible, interoperable, and reusable (FAIR) aspects. All supplementary materials have been prepared following best practices to ensure reproducibility, providing detailed instructions for any reader to replicate the results, subject to the necessary permissions to use the software employed in this study. Furthermore, upon publication of this article, a preprint version of its content will be deposited in my university's institutional repository, in accordance with standard institutional practice.

Supplementary information (SI): methodological aspects, full computational details. See DOI: https://doi.org/10.1039/d6cy00192k.

Acknowledgements

J. M. D.-R., R. Q.-C., and L. M. A. are grateful to MCIN/AEI and NextGenerationEU/PRTR for the financial support through project ref. PID2022-143294OB-I00. D. R. M. and A. N. S. acknowledge the financial support from the Australian Research Council (DP250102783). L. M. A. is a Ramón y Cajal fellow (ref. RYC2021-030994-I). Gratitude is also due to the KAUST Supercomputer Laboratory (KSL), KSA, for providing the computational resources (Shaheen III). This paper is dedicated to Prof Steve Scheiner (Utah State University) in recognition of his outstanding contributions to the study of non-covalent interactions.

Notes and references

1 D. R. MacFarlane, P. V. Cherepanov, J. Choi, B. H. R. Suryanto, R. Y. Hodgetts, J. M. Bakker, F. M. Ferrero Vallana and A. N. Simonov, *Joule*, 2020, **4**, 1186–1205.
2 H. Zhang, Z. Lu and Z. Wen, *Nat. Rev. Chem.*, 2025, **9**, 285–286.
3 J. M. McEnaney, A. R. Singh, J. A. Schwalbe, J. Kibsgaard, J. C. Lin, M. Cargnello, T. F. Jaramillo and J. K. Nørskov, *Energy Environ. Sci.*, 2017, **10**, 1621–1630.
4 S. Z. Andersen, M. J. Statt, V. J. Bukas, S. G. Shapel, J. B. Pedersen, K. Krempl, M. Saccoccio, D. Chakraborty, J. Kibsgaard, P. C. K. Vesborg, J. Nørskov and I. Chorkendorff, *Energy Environ. Sci.*, 2020, **13**, 4291–4300.
5 K. Li, S. Z. Andersen, M. J. Statt, M. Saccoccio, V. J. Bukas, K. Krempl, R. Sažinas, J. B. Pedersen, V. Shadravan, Y. Zhou, D. Chakraborty, J. Kibsgaard, P. C. K. Vesborg, J. K. Nørskov and I. Chorkendorff, *Science*, 2021, **374**, 1593–1597.
6 B. H. R. Suryanto, K. Matuszek, J. Choi, R. Y. Hodgetts, H.-L. Du, J. M. Bakker, C. S. M. Kang, P. V. Cherepanov, A. N. Simonov and D. R. MacFarlane, *Science*, 2021, **372**, 1187–1191.
7 H.-L. Du, M. Chatti, R. Y. Hodgetts, P. V. Cherepanov, C. K. Nguyen, K. Matuszek, D. R. MacFarlane and A. N. Simonov, *Nature*, 2022, **609**, 722–727.

8 D. R. MacFarlane, A. N. Simonov, T. M. Vu, S. Johnston and L. M. Azofra, *Faraday Discuss.*, 2023, **243**, 557–570.
9 L. M. Azofra, J. M. Doña-Rodríguez, D. R. MacFarlane and A. N. Simonov, *J. Phys. Chem. C*, 2025, **129**, 1198–1205.
10 T. Ludwig, A. R. Singh and J. K. Nørskov, *J. Phys. Chem. C*, 2020, **124**, 26368–26378.
11 Y. Abghoui, A. L. Garden, J. G. Howalt, T. Vegge and E. Skúlason, *ACS Catal.*, 2016, **6**, 635–646.
12 D. Wang, L. M. Azofra, M. Harb, L. Cavallo, X. Zhang, B. H. R. Suryanto and D. R. MacFarlane, *ChemSusChem*, 2018, **11**, 3416–3422.
13 B. H. R. Suryanto, D. Wang, L. M. Azofra, M. Harb, L. Cavallo, R. Jalili, D. R. G. Mitchell, M. Chatti and D. R. MacFarlane, *ACS Energy Lett.*, 2019, **4**, 430–435.
14 S. Kamiguchi, K. Asakura, T. Shibayama, T. Yokaichiya, T. Ikeda, A. Nakayama, K. Shimizu and Z. Hou, *Chem. Sci.*, 2024, **15**, 2914–2922.
15 Y. Jiang, Z. Chen, T. Peng, L. Jiao, X. Pan, H.-L. Jiang and X. Bao, *Angew. Chem., Int. Ed.*, 2025, **64**, e202501190.
16 S. C. Jesudass, S. Surendran, J. Y. Kim, T.-Y. An, G. Janani, T.-H. Kim, J. K. Kim and U. Sim, *Electrochem. Energy Rev.*, 2023, **6**, 27.
17 W.-Q. Li, M. Xu, J.-S. Chen and T.-N. Ye, *Adv. Mater.*, 2024, **36**, 2408434.
18 T. Žibert, B. Likozar and M. Huš, *ChemSusChem*, 2024, **17**, e202301730.
19 X. Fu, A. Xu, J. B. Pedersen, S. Li, R. Sažinas, Y. Zhou, S. Z. Andersen, M. Saccoccio, N. H. Deissler, J. B. V. Mygind, J. Kibsgaard, P. C. K. Vesborg, J. K. Nørskov and I. Chorkendorff, *Nat. Commun.*, 2024, **15**, 2417.
20 H.-L. Du, K. Matuszek, R. Y. Hodgetts, K. Ngoc Dinh, P. V. Cherepanov, J. M. Bakker, D. R. MacFarlane and A. N. Simonov, *Energy Environ. Sci.*, 2023, **16**, 1082–1090.
21 X. Fu, V. A. Niemann, Y. Zhou, S. Li, K. Zhang, J. B. Pedersen, M. Saccoccio, S. Z. Andersen, K. Enemark-Rasmussen, P. Benedek, A. Xu, N. H. Deissler, J. B. V. Mygind, A. C. Nielander, J. Kibsgaard, P. C. K. Vesborg, J. K. Nørskov, T. F. Jaramillo and I. Chorkendorff, *Nat. Mater.*, 2024, **23**, 101–107.
22 M. Krebsz, R. Y. Hodgetts, S. Johnston, C. K. Nguyen, Y. Hora, D. R. MacFarlane and A. N. Simonov, *Energy Environ. Sci.*, 2024, **17**, 4481–4487.
23 V. Azumah, L. Kavalsky and V. Viswanathan, *J. Phys. Chem. C*, 2025, **129**, 2488–2501.
24 V. Azumah, L. Kavalsky and V. Viswanathan, *J. Catal.*, 2025, **450**, 116250.
25 K. N. Wood, M. Noked and N. P. Dasgupta, *ACS Energy Lett.*, 2017, **2**, 664–672.
26 K. B. Hatzell, X. C. Chen, C. L. Cobb, N. P. Dasgupta, M. B. Dixit, L. E. Marbella, M. T. McDowell, P. P. Mukherjee, A. Verma, V. Viswanathan, A. S. Westover and W. G. Zeier, *ACS Energy Lett.*, 2020, **5**, 922–934.
27 K. Dong, Y. Xu, J. Tan, M. Osenberg, F. Sun, Z. Kochovski, D. T. Pham, S. Mei, A. Hilger, E. Ryan, Y. Lu, J. Banhart and I. Manke, *ACS Energy Lett.*, 2021, **6**, 1719–1728.
28 B. Hammer, L. B. Hansen and J. K. Nørskov, *Phys. Rev. B: Condens. Matter Mater. Phys.*, 1999, **59**, 7413–7421.
29 S. Grimme, J. Antony, S. Ehrlich and H. Krieg, *J. Chem. Phys.*, 2010, **132**, 154104.
30 S. Grimme, S. Ehrlich and L. Goerigk, *J. Comput. Chem.*, 2011, **32**, 1456–1465.
31 G. Kresse and J. Hafner, *Phys. Rev. B: Condens. Matter Mater. Phys.*, 1993, **47**, 558–561.
32 G. Kresse and J. Hafner, *Phys. Rev. B: Condens. Matter Mater. Phys.*, 1994, **49**, 14251–14269.
33 G. Kresse and J. Furthmüller, *Phys. Rev. B: Condens. Matter Mater. Phys.*, 1996, **54**, 11169–11186.
34 G. Kresse and J. Furthmüller, *Comput. Mater. Sci.*, 1996, **6**, 15–50.
35 B. H. R. Suryanto, C. S. M. Kang, D. Wang, C. Xiao, F. Zhou, L. M. Azofra, L. Cavallo, X. Zhang and D. R. MacFarlane, *ACS Energy Lett.*, 2018, **3**, 1219–1224.
36 L. M. Azofra, C. Sun, L. Cavallo and D. R. MacFarlane, *Chem. Eur. J.*, 2017, **23**, 8275–8279.